

# Path Planning Using Optically Computed Potential Fields

Max B. Reid

Photonics Group, Information Sciences Division  
NASA Ames Research Center

## Abstract

*An algorithm for the optical computation of potential field maps suitable for mobile robot navigation is described and experimentally produced maps and paths are presented. The parallel analog optical computation employs a two dimensional spatial light modulator on which an image of the potential field map is generated. Optically calculated fields contain no local minima, tend to produce paths centered in gaps between obstacles, and produce paths which give preference to wide gaps. Calculation of 128 x 128 pixel fields at a few hertz are possible with current technology, and calculation time vs. map size scales favorably in comparison to digital electronic computation.*

## 1: Introduction

An introduction to the field of autonomous robotic path planning may be found in Ref. 1. Here we consider one class of path planning problem, that of determining a series of motions for a robot to execute in order to move from an initial location to a designated goal location in a bounded two dimensional workspace. Figure 1a shows a view from above of such a workspace, which could be a room bounded by walls and containing furniture of various shapes.

We consider here the method of path planning using artificial potential fields, which takes its name from its use of an analogy to electrostatic potentials [2-7]. Each location in the workspace is considered to have an associated potential energy  $U(x)$ . In practice, the workspace is often divided into some finite number of cells, as in Fig. 1b. Each cell has a distinct potential value and the robot moves from cell to cell. The robot is assumed to follow the gradient of the potential, responding to the force

$$\mathbf{F}(x) = -\nabla U(x). \quad (1)$$

Other more sophisticated algorithms for choosing the path have been developed [1]-[7], but in all cases, a method is required to calculate a potential value for any

location in the workspace. Generally, the field throughout the workspace due to each obstacle and the goal are calculated separately and then added to produce a potential field map for the entire workspace. The actual functional form of the separate  $U$ 's can follow the electrostatic analogy of a field which is inversely proportional to distance, but more usually, the form of  $U(r)$  is not exactly  $1/r$ , but some other monotonically decreasing function [1],[5]-[7].

The biggest drawback of the potential field approach is that it often produces local minima which can trap the robot before it reaches the goal [1]. For example, at a point directly behind an obstacle from the goal, the force on the robot may be either directly away from or towards the obstacle, or the robot may reach a local minimum where the forces exactly cancel. A second problem can arise due to the use of positive potential field contributions from obstacles. Those edges of obstacles which are close together can form a high potential ridge with a local minimum between them.

A recent technique avoids local minima by computing potential values for the entire workspace as a system, instead of adding together individual contributions from goal and obstacles [8]. The obstacles are still maximum potential locations, but they have no field which extends beyond their boundaries. The goal location, rather than being considered the center of a

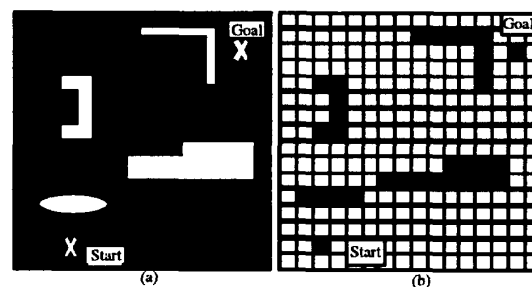


Figure 1: Bounded two dimensional workspace containing obstacles. a) Example initial and goal locations for a mobile robot are shown. b) Workspace and obstacles divided into a finite number of resolution cells.

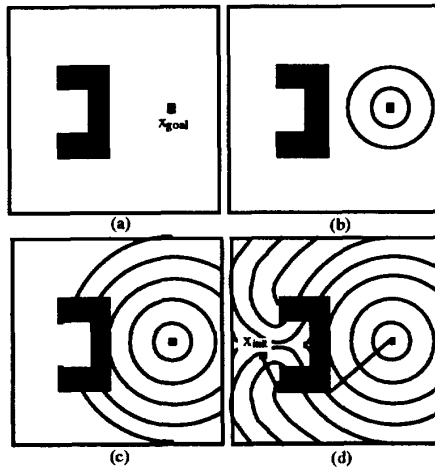


Figure 2: Potential field map calculation algorithm employing expanding goal region. a) Initial goal and obstacle locations. b) First two equipotential lines show expanding goal region. c) Expanding goal region is forced to proceed around obstacles. d) Final equipotential map. Highest potentials are directly behind the obstacle.

radially symmetric function such as (1), is the source of an expanding low potential region which starts in a small area and grows uniformly until it reaches an obstacle. Upon reaching an obstacle, the goal's "field" spreads around the obstacle. The field stops expanding when it has filled the entire workspace. Figure 2 shows the steps in this process. In Fig. 2b the first two equipotential lines surrounding the goal are shown. In this algorithm, each equipotential line is separated by an equal distance. After the obstacle is reached, the equipotential lines are no longer radially symmetric, but are distorted in going around the object, as shown in Fig. 2c. The completed pattern in Fig. 2d contains no local minima, and a robot located behind the obstacle will be guided around it, following a path such as that shown in the figure. In a conventional digital electronic implementation, this algorithm runs in  $O(N^{3/2})$  time, where  $N$  is the number of cells [8]. Alternative techniques for overcoming local minima are even more computationally intensive [1],[5],[6].

The large amount of computation required to produce paths which are not distorted by local minima is a general drawback of the potential field technique. A rapid method of calculating local-minima-free potential field maps is required to facilitate dynamic path re-planning. In this work, a method for producing local-minima-free potential field maps is proposed and demonstrated experimentally using analog optical computation. The inherently parallel nature of the optical calculation makes it especially well suited for handling large, high-resolution workspaces.

## 2: Optical calculation of potential fields

High speed analog optical computation of field maps suitable for robotic path planning can be performed using a microchannel spatial light modulator (MSLM). The MSLM is a device used to produce two dimensional optical images with gray-scale intensity values [9]-[11]. Commercial versions of the MSLM [12] have been utilized in a variety of optical computing applications.

### 2.1: MSLM operation

A diagram of the MSLM is shown in Fig. 3. The device consists essentially of a photocathode, a microchannel plate (MCP), and an electrooptic crystal. An input light intensity distribution is converted by the photocathode to a spatial electronic current distribution, which is then amplified by the MCP and deposited on the crystal, typically  $\text{LiNbO}_3$ . The electrooptic crystal is coated with a thin dielectric mirror. The deposited surface charge density,  $\sigma_s$ , creates an electric field across the electrooptic crystal. The polarization of a coherent readout light beam which passes twice through the electrooptic crystal is rotated by this electric field via the Pockels effect [13], and the spatial distribution in  $\sigma_s$  is converted to an amplitude distribution in the readout beam through the use of a polarizer.

There are two basic methods which can be used to write spatial patterns onto the MSLM. The first is through electron deposition onto the dielectric mirror as described above. The second method involves first depositing a uniform charge distribution on the surface of the mirror and then removing, or depleting, charge from areas to be written. Figures 4a and 4b show the results of writing a simple square pattern in the two modes. In both cases the pattern was written up to a point of  $\approx 90\%$  amplitude modulation. At this level of modulation, the two patterns are very nearly reverse contrast images. However, if the electron deposition/depletion process is continued, the deposited pattern begins to expand, while the depleted pattern remains relatively confined, as shown in Figures 4c and 4d [14],[15].

### 2.2: Potential field computation algorithm

In the introduction we saw an algorithm for computing local-minima-free potential field maps which

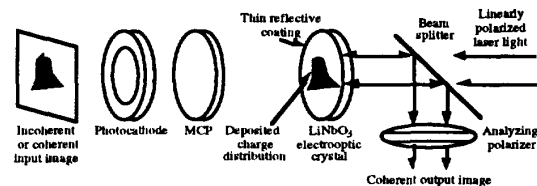


Figure 3: Basic operation of the microchannel spatial light modulator (MSLM).

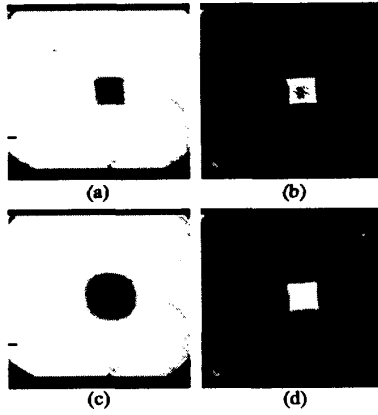


Figure 4: Behavior of MSLM electron deposition and electron depletion writing modes. a) Square pattern written for time  $t_1$  to 90% modulation in deposition mode. b) Same pattern written for time  $t_2$  to 90% modulation in depletion mode. c) Pattern written for  $3t_1$  in deposition mode. d) Pattern written for  $3t_2$  in depletion mode.

involved distinct, sharp edged obstacles and an expanding goal area. The two write modes of the MSLM may be used to implement both types of behavior, following the algorithm diagrammed in Fig. 5. Let the workspace be represented by the output pattern of the MSLM. The workspace is initially uniformly written in depletion mode and then the goal is written in deposition mode. At this point, an image of the MSLM output shows the goal at a value of zero (black in Fig. 4), while the remaining area of the workspace is at the maximum 8-bit gray-scale value of 255 (white in Fig. 4).

A series of alternating deposition/depletion writing cycles follows. The goal region is written for a time  $t_e$ , during which time the deposited region expands. During each electron deposition step, we illuminate the photocathode in all areas into which the goal region expanded in previous cycles. When the expanding deposited area reaches the location of an obstacle, some of the deposited electrons fall within the borders of the obstacle. This charge is removed by writing in depletion mode for a time  $t_p$ . All obstacles are written back to full intensity before an image is taken of the output pattern.

The procedure terminates after the area written via electron deposition spreads to cover the entire active area of the electrooptic crystal, excluding the regions occupied by obstacles. When the workspace is fully written, output images no longer change and the cycle is stopped. The potential field map is formed by averaging the images taken at the end of each write cycle and should contain no local minima. Any electrons which spread into the bounds of obstacles are removed, while electrons which spread around the edges of the obstacles are

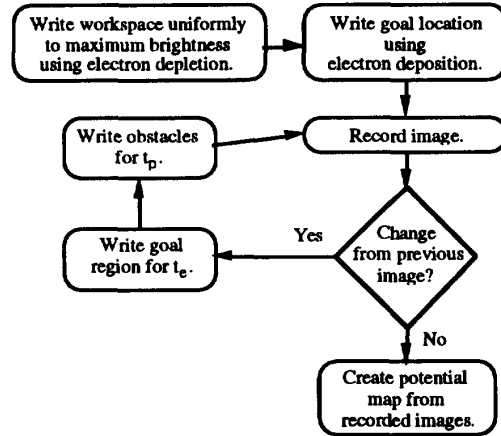


Figure 5: Algorithm for optical calculation of potential field map. Goal region is written on MSLM using electron deposition. This region expands from its initial location to fill the entire workspace. Obstacles are periodically rewritten using electron depletion, forcing the goal region to expand around the obstacles.

allowed to accumulate. Eventually, the deposited area spreads around obstacles, creating a potential map similar to Fig. 2d.

### 2.3: Calculation time

We derive the total optical writing time required to complete a potential field calculation and then compare the scaling of computation time with the size of the robot's workspace for both the electronic and the optical operations in the algorithm diagrammed in Fig. 5. The overall limiting factor for system speed is compared to the speed of conventional digital electronic systems.

**2.3.1: Derivation of optical writing time:** First we consider the time required for the goal region to spread across the entire active area of the MSLM crystal. Assuming a uniform intensity write beam limited by an aperture of area  $A$ , the charge deposited in a time  $\Delta t$  fully modulates an area given by [14],[15]

$$\Delta A = \frac{\Delta Q}{\sigma_{\pi/2}} = \frac{J_p A \Delta t}{\sigma_{\pi/2}}, \quad (2)$$

where  $Q$  is the total charge deposited on the electrooptic crystal,  $\sigma_{\pi/2}$  is the charge density required to produce full amplitude modulation of a readout light beam passing twice through the crystal [12], and  $J_p$  is the electron current density emitted by the MCP. For short writing time intervals,  $\Delta A$  is much smaller than  $A$ , and (2) represents exponential growth in  $A$ . The time required for the goal region to grow from the size of one

resolution cell,  $A_0$ , until it fills the entire crystal active area,  $A_m$ , is therefore given by

$$t_m = \frac{\eta \sigma \pi/2}{J_p} \ln\left(\frac{A_m}{A_0}\right), \quad (3)$$

where the periods of electron depletion writing during which obstacles are rewritten are included by the factor  $\eta = (t_e + t_p)/t_e$ .

When obstacles are present, some of the charge accumulated during deposition mode writing is deposited in obstacle regions. This charge is removed during subsequent depletion mode rewriting of obstacles, and it does not contribute to modulating all of the obstacle-free regions of the active area. This is reflected in our final equation for optical writing time

$$t_{\text{calc}} = \frac{\xi \eta \sigma \pi/2}{J_p} \ln\left(\frac{A_m}{A_0}\right), \quad (4)$$

where  $\xi$  is a factor greater than one which is dependent on the specific number, size and placement of obstacles in the workspace, and on the position of the goal.

The speed of the optical calculation is limited primarily by the maximum current of the microchannel plate,  $J_p$ . Using the highest value of  $J_p$  demonstrated to date in (4) results in a value for  $t_{\text{calc}}$  of a few tenths of a second, allowing potential field map updates at a few hertz. MSLMs with higher current densities are feasible.

**2.3.2: Write cycle frequency:** The derivation of optical writing time includes both periods of deposition mode writing lasting  $t_e$  and depletion mode writing for periods of  $t_p$ . Specific writing durations were not used in deriving  $t_{\text{calc}}$ , although they were assumed to be much shorter than  $t_{\text{calc}}$  in the derivation of (3). The limit on write cycle duration is determined in practice by the phenomenon we refer to as "breaching". If the area written in deposition mode is allowed to expand too much before the obstacles are rewritten, deposited electrons can spread completely across an obstacle. The charge which is deposited behind the obstacle remains after the obstacle is rewritten and leads to creation of a local minimum in the final potential field. Breaching does not occur if the total amount of charge deposited during  $t_e$  is sufficiently small. The total number of deposition/depletion write cycles is given by

$$M = \frac{t_{\text{calc}}}{\eta t_e}. \quad (5)$$

For the obstacles patterns considered in the following section, we find empirically that  $M$  must be on the order of 100 to avoid breaching.

**2.3.3: Scaling of system calculation time:** In addition to calculation speed, we are interested in total computational throughput. The value for  $t_{\text{calc}}$  computed in Section 2.3.1 is for a potential field with  $128 \times 128$  pixel resolution. As the number of resolution cells,  $N$ , is given by  $A_m/A_0$ , we see from (4) that the optical writing time scales as  $\ln(N)$ . The full potential field calculation algorithm of Fig. 5 includes electronically implemented functions such as image recording. Each of these operations scales linearly with the size of images, i.e., as  $O(N)$ . In addition, each of these operations is repeated  $M$  times during the calculation of a potential field map, where  $M$  scales as  $O(\ln N)$  from (4) and (5). The electronic operations therefore determine the ultimate limit on system computation speed. In the limit of large  $N$ , the order of the computation time for the hybrid optical/electronic system is  $O(N \ln(N))$ .

We discussed in Section 1 that comparable potential field map computations performed using conventional digital electronics scale at best as  $O(N^{3/2})$ . The advantage of optical calculations therefore lies in the domain of large, high resolution potential field maps. For the optical implementation,  $N$  may be increased either by increasing the active area of the crystal or by increasing the crystal resolution.

### 3: Experimental results

The optical potential field computation algorithm of Fig. 5 was tested on both single and multiple obstacle workspaces. The experimental apparatus is described in detail in [14] and [15].

#### 3.1: Single obstacle workspace

A "C" or "U" shaped obstacle commonly used in robotics research [1] was used to demonstrate the procedure in the single obstacle case, as shown in Fig. 6a. This type of object is difficult for many path planning algorithms to handle because of the creation of local minima behind or in the inner space of the obstacle. Five intermediate output images taken during the execution of the algorithm are seen in Fig. 6, starting just after the goal was written in Fig. 6b. Output images after 20, 40, 60, and 80 write cycle iterations are shown in Figures 6c-f. In Fig. 6c, the goal region has just expanded to the edge of the obstacle. The deposited area spreads around the obstacle in Figures 6d and 6e, and has almost filled the entire workspace in Fig. 6f. The value of the obstacle-dependent factor in the optical writing time of (4) was measured to be  $\xi = 1.7$ .

After the output image stopped changing, the sequence of images stored during the writing process was averaged to produce the potential field map. The potential field map is a gray-scale image with values ranging from 0 at the goal to 255 within the bounds of the obstacle. Figure 7a shows a contour plot where the

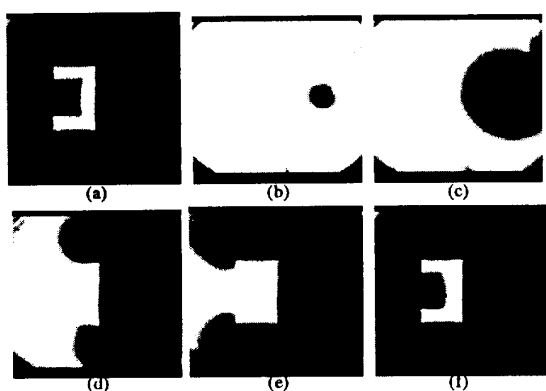


Figure 6: Intermediate MSLM output images taken during optical potential field calculation. a) "C" shaped obstacle. b) Initial goal pattern. c) Output after 20 iterations of deposition/depletion write cycle. d) 40 iterations. e) 60 iterations. f) 80 iterations.

first equipotential line surrounding the goal represents a gray-scale value of 15, and each successive line is separated by a gray-scale value of 16. Notice that the highest potential values in the field are those directly behind the obstacle from the goal. We have simulated the path that a simple "point robot" would follow when started at any initial position in the workspace. A point robot is assumed to occupy only one resolution cell of the workspace at a time. The robot follows the potential map using simple gradient descent without momentum.

An example path is shown in Fig. 7b, where the robot is assumed to begin at a location which is behind the obstacle in this case. It then follows a path roughly perpendicular to the equipotential lines. The robot successfully proceeds around the obstacle and reaches the goal without being trapped by any local minima. In addition, the optically calculated potential field does not result in a path which follows the exact edge of the obstacle. Some potential field calculation algorithms generate paths which follow obstacle boundaries so closely that a robot with spatial extent beyond one resolution cell would collide with the obstacles (see Fig. 2d).

### 3.2: Multiple obstacle workspace

An optical potential field calculation was also performed for the workspace shown in Fig. 8a, which contains four obstacles. In this case the dependence of the calculation time in (4) on the obstacle pattern was measured to be  $\xi = 3.1$ . Five output images taken during the writing process are shown in Figures 8b-f. The dark area in the upper righthand corner in Figures 8c-e is due to a defect in one of the optical components.

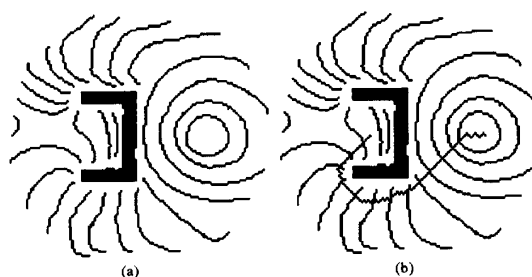


Figure 7: Optically calculated potential field for "C" obstacle. a) Equipotential contour plot of gray-scale field map. b) Path followed by a simulated "point robot" using simple gradient descent through the optically calculated potential field map. Path is roughly perpendicular to equipotential lines.

The composite potential field map is seen in Fig. 9a. The goal region expands most quickly in areas where there are large gaps between obstacles. Near small gaps, a larger percentage of electrons are deposited in obstacle regions and are subsequently removed, resulting in slower spread of the deposited area. Faster spread through large gaps yields potential field maps which favor robot paths between widely separated obstacles over paths of equal length between closely spaced obstacles. In many cases, especially for non-point, extended robots, this may be a desirable behavior.

An example is shown in Fig. 9b, which plots two paths generated by following the potential field map

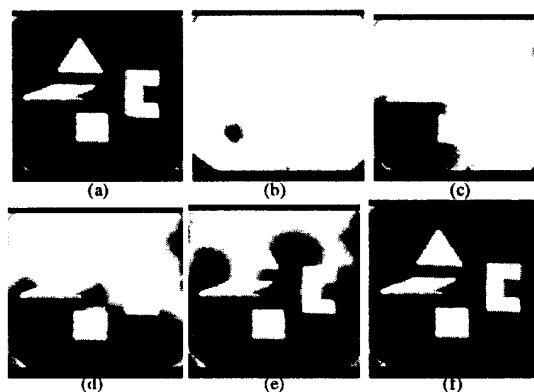


Figure 8: Intermediate MSLM output images taken during optical potential field calculation process for four-obstacle workspace. a) Workspace containing triangle, "C", square and parallelogram obstacles. b) Initial goal pattern. c) Output after 40 iterations of deposition/depletion write cycle. d) 80 iterations. e) 120 iterations. f) 156 iterations.

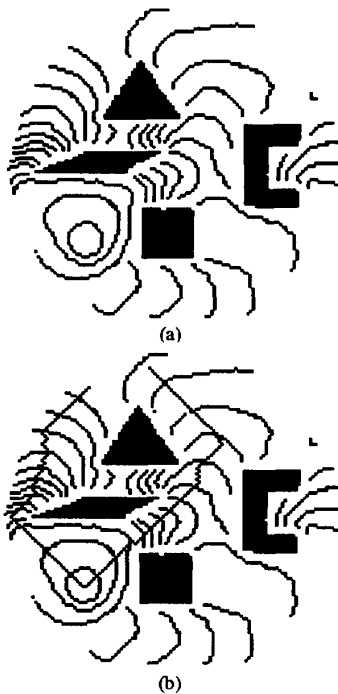


Figure 9: Optically calculated potential field for four-obstacle workspace. a) Equipotential contour plot of gray-scale potential field map. b) Two paths with different starting positions followed by a simulated "point robot" using simple gradient descent.

using a simple gradient descent planning algorithm. The charge deposited region spread around the triangular obstacle from two different directions, forming a relatively high potential ridge above and to the left of the triangle. A robot placed on one side of the ridge follows a path in one direction around the triangle and parallelogram, while a robot placed on the other side of the potential ridge follows a path in a different direction. The optically generated field map does not guarantee an optimally short path, but it does implicitly weigh the benefits of path length and path width and produces a path which represents a compromise between these parameters.

#### 4: Conclusions

We have experimentally shown that a microchannel spatial light modulator (MSLM) can be used to perform analog optical calculations of local-minima-free potential field maps suitable for robotic path planning. Optics is well suited for this application because the hybrid optical/electronic calculation scales as  $O(N \ln(N))$ , where  $N$  is the number of resolution cells in the robot's workspace, whereas conventional digital electronic

techniques scale as  $O(N^{3/2})$  or worse. In addition, optically calculated potential fields have the often desirable characteristics of producing paths through the middle of gaps between obstacles and paths which give preference to wide gaps.

Map updates at several hertz for  $128 \times 128$  pixel fields are feasible using existing MSLM technologies. The bandwidth of optical potential field calculations may be increased further by increasing the area of the electrooptic crystal, by increasing the maximum current density of the microchannel plate, and by decreasing the electrooptic crystal thickness.

#### References

1. J.C. Latombe, *Robot Motion Planning*. Boston: Kluwer Academic Publishers, 1991.
2. O. Khatib, "Real-time obstacle avoidance for manipulators and mobile robots," *Int. J. Robotics Research*, vol. 5, pp. 90-98, 1986.
3. F. Miyazaki and S. Arimoto, "Sensory feedback based on the artificial potential for robots," in *Proc. 9th IFAC*, Budapest, 1984.
4. V.V. Pavlov and A.N. Voronin, "The method of potential functions for coding constraints of the external space in an intelligent mobile robot," *Soviet Automat. Control*, vol. 6, 1984.
5. D.E. Koditschek, "Exact robot navigation by means of potential functions: some topological considerations," *Proc. IEEE Int. Conf. Robotics and Automation*, Raleigh, NC, pp. 1-6, 1987.
6. J. Barraquand and J.C. Latombe, "Robot motion planning: a distributed representation approach," *Int. J. Robotics Research*, vol. 10, pp. 628-649, 1991.
7. Y.K. Hwang and N. Ahuja, "A potential field approach to path planning," *IEEE Tran. Robotics and Automat.*, vol. 8, pp. 23-32, 1992.
8. E.S. Plumer, "Neural network structure for navigation using potential fields," in *Proc. Int. Joint IEEE/INNS Conf. on Neural Networks*, Baltimore, June 7-11, 1992.
9. C. Warde, A.D. Fisher, D.M. Cocco, and M.Y. Burmawi, "Microchannel spatial light modulator," *Opt. Lett.*, vol. 3, pp. 196-198, 1978.
10. A.D. Fisher, "Techniques and devices for high-resolution adaptive optics," Ph.D. dissertation. Cambridge, Mass.: Massachusetts Institute of Technology, 1981.
11. C. Warde and J. Thackara, "Operating modes of the microchannel spatial light modulator," *Opt. Eng.*, vol. 22, pp. 695-703, 1983.
12. T. Hara, Y. Ooi, Y. Suzuki, and M.H. Wu, "Transfer characteristics of the microchannel spatial light modulator," *Appl. Opt.*, vol. 28, pp. 4781-4786, 1989.
13. A. Yariv, *Introduction to Optical Electronics*, 2nd ed. New York: Holt, Rinehart, Winston, 1976, pp. 246-253.
14. M.B. Reid, "Calculating potential fields using microchannel spatial light modulators," in *Proc. SPIE*, vol. 1772, 1992, paper # 29.
15. M.B. Reid, "Optical calculation of potential fields for robotic path planning," submitted to *Appl. Opt.*